JOURNAL OF AIRCRAFT
Vol. 37, No. 2, March–April 2000

Effects of Anhedral and Dihedral on a 75-deg Sweep Delta Wing

Lance W. Traub[*]
Texas A&M University, College Station, Texas 77843-3141

An investigation into the effects of spanwise camber in the form of anhedral and dihedral on a 75-deg sweep delta wing is detailed. Data are presented encompassing force balance, surface pressure measurement, seven-hole probe surveys, and vortex burst trajectories. The results show that the net effect of this form of nonplanarity is an increase in lift for anhedral and a decrease in lift for dihedral compared to the planar wing. Small anhedral angles are most effective in augmenting lift. Anhedral does not appear to greatly augment the strength of the leading-edge vortex. The major benefit from anhedral would appear to be due to its displacing effect on the vortex trajectory: drawing the vortex closer to the wing surface and inboard compared to the planar wing. As the vortex is drawn inboard, its induced surface loading acts on a greater area of the wing. Dihedral also draws the vortex closer to the wing surface (to a greater extent then anhedral) while moving the vortex toward the wing leading edge. In addition, anhedral does not appear to introduce any detrimental effects on longitudinal stability and does not incur any penalties in terms of vortex burst characteristics.

Nomenclature

$C_{D\,\min}$ = minimum drag coefficient
C_L = lift coefficient
C_N = normal force coefficient
C_{pt} = maximum stagnation pressure loss
C_T = leading-edge thrust coefficient
c_r = wing root chord
k = wing efficiency parameter
k_P = potential lift constant
q = freestream dynamic pressure
r = radial coordinate, measured from vortex center line
s = local semispan
U = freestream velocity
V_A = axial velocity
V_θ = rotational velocity
v, w = spanwise velocity, vertical velocity normal to wing surface
x, y, z, y', z' = Cartesian coordinates, y' and z' orientated at ϕ
α = wing centerline incidence
Γ = vortex circulation
Λ = wing leading-edge sweep angle
ϕ = wing dihedral angle, defined $(-)$ for anhedral, $(+)$ for dihedral
ω = axial vorticity

Subscripts

max = maximum
min = minimum
np = nonplanar
pr = projected

Introduction

DELTA, or triangular wings, were first tested by Winter in 1935.[1] Because of the ability of the delta-wing planform to satisfy the disparate requirements of low wave drag at supersonic speed and stable and controllable flight at high α, a considerable number of studies have been undertaken to elucidate their flow characteristics. Generally, the flow mechanism and physics of delta wings are well understood.

For a delta wing with sharp leading edges, enforcement of the Kutta condition at the leading edge ensures that the flow separates, forming leading-edge vortices. These structures are fed from the vorticity generated by the merging of the upper and lower surface leading-edge boundary layers. The velocity vectors on the upper and lower surfaces of the wing leading edge are equal in magnitude, but have different orientations yielding a resultant vorticity vector closely aligned with the wing leading edge. The merging boundary layers form a free shear layer or vortex sheet that rolls up to form a vortex with a viscous core surrounded by an essentially inviscid rotational region bounded by the free shear layer. Remnants of the spiraling free shear layer are usually not apparent in the vortex structure due to diffusion of vorticity attenuating the vorticity gradients.

Delta wings are not without limitations. They are poor lift generators because of their low AR, requiring high α (with consequent high drag) for takeoff and landing. If the delta wing is sharp-edged or the flow has separated, lift is augmented by the leading-edge vortices, which induce high velocities on the wing upper surface, thereby reducing the surface pressure. This vortex lift, as shown by Polhamus,[2] is equal to the leading-edge suction that would have been developed if the flow on the wing was fully attached. Thus, the net effect of enforcing leading-edge flow separation on a flat delta wing is to cause effective rotation of the leading-edge suction force to the plane of the normal force. Naturally this is at the expense of a substantial increase in drag, as the leading-edge suction is lost. Nonetheless, as shown by Lamar[3] theoretically and experimentally, the substantial lift increases due to the leading-edge vortices, augmented through entrainment resulting from the core pressure deficit, can result in significant increases in wing efficiency, as lift is markedly increased for a given α.

Numerous devices and design methodologies have been tested with the purpose of enhancing the performance of delta wings, essentially by reducing drag. An initial concept, first proposed and successfully demonstrated by Lee,[4] is that of using a warped leading edge upon which to concentrate the vortex suction peak and so generate thrust. This concept has been greatly developed culminating in the leading-edge vortex flap (LEVF).[5–7] These devices are formed by rotating a leading-edge flap either above or below the plane of the wing. They differ from conventional leading-edge flaps in that they are not intended to suppress separation, but rather they concentrate the induced suction of the leading-edge vortex on the flap. As a consequence, drag of the wing is reduced if the flap is rotated below the plane of the wing. Lift, however, is also diminished, due to a reduction in vortex strength and a moderate reduction of

---

Received 28 May 1999; revision received 6 October 1999; accepted for publication 8 October 1999. Copyright © 1999 by Lance W. Traub. Published by the American Institute of Aeronautics and Astronautics, Inc., with permission.

[*] Postdoctoral Research Associate, Aerospace Engineering Department. Associate Member AIAA.

the attached flow lift component. As the flaps provide leading-edge camber, they shift the angle of attack for zero lift positive, so additionally reducing lift for a given α below stall. This effect does however result in improved high α performance as the maximum lift coefficient peak occurs at higher α.[6] Performance of a wing with vortex flaps improves overall, as the reduction in drag outweighs the loss of lift. LEVF performance is limited by the inboard migration and expansion of the leading-edge vortices with incidence. This may result in the flap effectively loosing the vortex suction as the vortex moves inboard, with a consequent drag penalty. For a planar wing with a constrained span, Munk[8] has shown that the minimum induced drag occurs when the downwash in the wake is constant. This condition for minimum drag for a given AR corresponds to that of elliptic spanwise loading. For minimum drag the wing should have a large span to capture as great a volume of air as possible, thus requiring less work to accelerate it downward to generate the lift impulse. If the wing is not constrained to be spanwise planar, Cone[9] and Lowson[10] have shown that numerous nonplanar wing forms (wings with spanwise camber of their lifting lines, e.g., V wings, end plates, etc.) can improve efficiency beyond the theoretical planar minimum. Nonplanarity has numerous effects on the aerodynamics of the wing. The curve of the spanwise cambered bound vortex results in an incremental induced velocity parallel to the freestream, so-called induced lift. This effect is not symmetrical with respect to anhedral or dihedral. Cone[9] shows that the induced drag of a lifting system can be varied by changing the spatial distribution of the trailing vorticity. To reduce the effective downwash (and thus induced drag), the strength of the trailing vorticity should be minimized, and the lifting elements should be distributed over a large area. For a planar wing this may be achieved by increasing the wing span for a given lift coefficient and by distributing the trailing vorticity over a large vertical area for a nonplanar system. The underlying principle is that by spreading the vorticity for a given lift a larger mass of air is affected, and consequently the velocity at a point is lowered so by reducing the wake velocities.

The wing efficiency factor may be expressed as $k = \pi \mathrm{AR}(C_D - C_{D\,\mathrm{min}})/C_L^2$, where $C_D = C_N \sin\alpha - C_T \cos\alpha$. This expression shows that for a given wing aspect ratio wing efficiency may be increased (i.e., minimize k) by enhancing leading-edge or camber thrust, or by increasing the lifting ability of the wing (for a given α), or a combination of both. For a sharp-edged wing, with no chordwise camber, $k = \pi \mathrm{AR} \tan\alpha / C_L$ as $C_D - C_{D\,\mathrm{min}} = C_L \tan\alpha$. Thus in this case k may be reduced only by increasing the lifting ability of the wing for a given α. Spanwise camber, through reduced downwash and/or enhanced vortex lift, may provide a means to improve efficiency for this type of wing configuration.

Experimental investigations of cambered delta wings have often been limited to those with conical camber so as to afford comparison with available prediction methodology. However, conically cambered delta wings contain both chordwise and spanwise camber effects. A notable experimental investigation on camber effects was the study of Squire.[11] Squire's investigation was motivated in part by the observation that wind-tunnel tests of certain conically cambered gothic wing forms for a supersonic transport aircraft generated lift curve slopes larger than the planar equivalent at lift coefficients above that of leading-edge flow attachment. Squire's test cases consisted of a $\Lambda = 76$-deg wing ($\mathrm{AR} = 1$) with various leading-edge droop angles and shoulder locations. Significant, however, in his study was the inclusion of a delta wing with pure anhedral of 16.7 deg such that the wing possessed no chordwise camber. Squire's results showed that leading-edge camber does indeed increase the lift curve slope of the wing above the attachment incidence but shifts the angle of attack for zero lift positive. An exception to this was the result for the delta with pure anhedral. As this wing had no chordwise camber, the angle of attack for zero lift occurred at $\alpha = 0$ deg. The results exhibited a substantial increase in lift beyond the projected planar wing, with an increase in lift of 11% at $\alpha = 16$ deg. Squire attributed the lift increase, based on results from the theoretical model of Brown and Michael,[12] to "the distortion of the velocity field of the vorticity which is produced by the curvature of the wing in the cross-flow plane." Squire's theoretical modeling suggested that the effect of conical camber was to increase the height of the vortex core above the wing leading-edge and increase its strength. In the transformed plane, in which computations are performed in the Brown and Michael method, Squire noted that the vortices were closer to the wing surface, thus increasing the upper surface crossflow velocities and hence reducing pressure. In the physical plane the converse was true, leading Squire to conclude that wing camber produces a large distortion of the flowfield around the vortices.

Early experimental studies of dihedral on swept wings were primarily concerned with stability effects.[13,14] Washburn and Gloss[15] investigated the effect of circular arc spanwise camber on a 76-deg sweep delta. Their results indicated that for this wing planform and camber distribution anhedral and dihedral had an insignificant effect on the vortex and its burst location. A subsequent study be Washburn and Gloss[16] focused on the effects of anhedral and dihedral on the longitudinal and lateral characteristics of a supersonic cruise configuration. Their results showed that for the configuration (which resembled a cranked arrow wing) studied longitudinal forces were relatively invariant, with the anhedral model showing a slight lift improvement. Lateral data were similar for all of the model variations.

The single result of Squire[11] for an $\mathrm{AR} = 1$ delta with 16.7-deg anhedral suggests that this type of pure spanwise cambering may offer a means to enhance performance without the limitations of LEVFs. Spanwise cambered wings would not suffer a significant zero lift drag penalty. Expansion and migration of the vortices would not impact performance. As the wing would not be optimized for a specific condition, it should have a flexibility in the flight envelope of efficient operation. The increment in lift noted by Squire[11] for the anhedral delta over the equivalent span planar wing could only be matched by increasing the planar wing's AR. In a high AR wing this would have the penalty of increased wing root bending moment; however, the penalty in slender wings is associated with the onset of vortex breakdown (BD). Increasing the wing's AR so as to enable it to match the lift increase would result in earlier BD, with all of its concomitant implications. Furthermore as noted by Washburn and Gloss,[15] for a wing planform (if not anhedral distribution) similar to Squire's[11] anhedral appeared to have a marginal effect on BD. Data pertaining to the effect of anhedral on delta wings are also useful for prediction of the behavior of caret wing configuration wave riders, as these types of aircraft would operate subsonically during takeoff and landing.

The present study was thus motivated by the lack of a systematic investigation of the effects of pure spanwise camber on delta wings. In this paper the form of the spanwise camber was limited to anhedral and dihedral, such that in a crossflow plane the wings formed a "∨" or "∧." The experimental investigation used a series of flat-plate delta wings with $\Lambda_{\mathrm{pr}} = 75$ deg. Anhedral/dihedral angles varying from 10 to 25 deg in 5-deg increments were used. The present investigation includes force-balance measurements, surface-pressure measurements, vortex-burst trajectories, and flowfield surveys using a seven-hole probe.

Model Description and Experimental Procedure

Figure 1a shows geometric details of the models used in the study. All of the wings were fabricated from mild steel plate. Kegelman and Roos[17] have shown that the leading-edge details (e.g., form of beveling, etc.) can dramatically affect the high α aerodynamics of the wing, determined experimentally using a series of wings 1.77% thick. Wentz and Kohlman,[18] however, found for a thinner series of wings (thickness/$c_r = 1.1\%$) that a square-edged wing showed similar performance characteristics to a chamfered or beveled edged wing. Consequently, to eliminate the necessity of beveling the wing's leading edges, they were manufactured from 1.52-mm-thick steel plate. The wing's thickness combined with a root chord of 375 mm yields a thickness to chord ratio of 0.41%. A projected leading-edge sweep angle of 75 deg was investigated. For each wing the projected span, and consequently the aspect ratio, were constrained, and thus the arc length of the wing was variable. This is in accordance with Cone,[9] who has shown that in comparing planar and nonplanar wings the use of the projected AR is

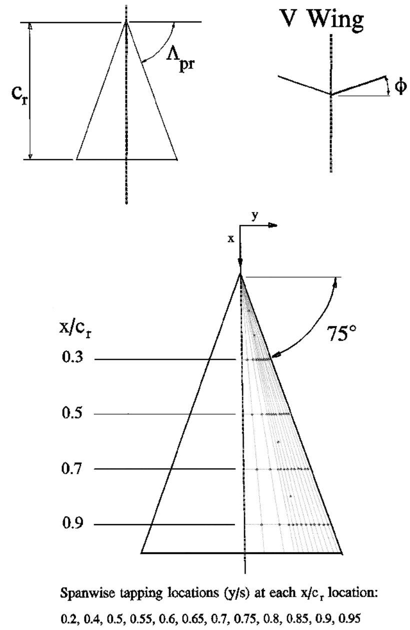

a) Model and pressure tapping locations

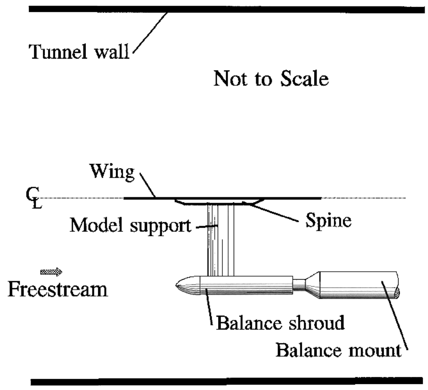

b) Model mounting system

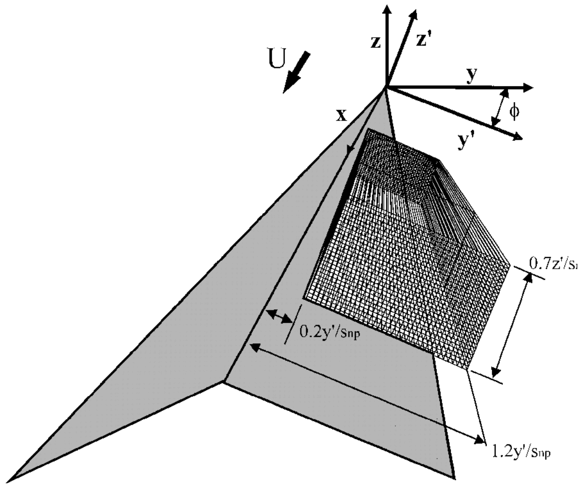

c) Grid geometry

Fig. 1 Wind-tunnel model, mount and flowfield survey grid geometrical details.

appropriate. Dihedral/anhedral angles of 10, 15, 20, and 25 deg were used.

The effects of anhedral/dihedral on the wing surface-pressure distribution were also investigated. Two wings, one planar with a leading-edge sweep angle of 75 deg and one nonplanar with an anhedral angle of 15 deg and a projected leading-edge sweep angle of 75 deg, were pressure tapped with a total of 52 taps per wing half. The tappings were distributed in four spanwise rows as shown in Fig. 1a. Tappings were also located along a ray at 65% of the local semispan, as this location is roughly coincident with the trajectory of the vortex core. The pressure tappings had a diameter of 0.5 mm, which should minimize errors in regions of large gradients.

The wings were attached to a mount that consisted of a thin reinforcing spine that extended for 203 mm along the root chord of the wing, so as to minimize wing flexing (see Fig. 1b). The model dimensions were kept to a minimum to reduce the effect of the wind-tunnel walls. Tests were undertaken in Texas A&M University's 3 × 4 ft continuous wind tunnel at $U = 45$ m/s and $Re = 1.14 \times 10^6$ based on c_r, unless mentioned otherwise.

Vortex-burst trajectories were determined in Texas A&M University's 2 × 3 ft water tunnel. These tests were run at a freestream velocity of 0.4 m/s, yielding a root chord Reynolds number of 0.15×10^6. Spanwise distance markers were drawn on the upper wing surface at 7-mm intervals allowing determination of the vortex burst location to within ≈ 1% of the wing root chord. Dye was injected at the wing apex to help locate the leading-edge vortices. The dye flow rate was controlled using a needle valve. Video footage was recorded during the tests and analyzed subsequently to determine the trajectories. The spiral vortex breakdown mode was seen to predominate, and the location of breakdown was taken as that at which the vortex core filament showed the distinctive kink associated with this mode.

Surface pressures were measured for an α range of 5–30 deg in 5-deg increments, as well as at $\alpha = 40$ deg for a projected wing sweep of 75 deg with $\phi = 0$ and -15 deg. Data were acquired at $U = 45$ m/s, yielding $Re = 1.14 \times 10^6$. The pressures were recorded at the four rows of spanwise tappings using a 48-port Scanivalve pressure multiplexer connected to an Air Neotronics autozeroing digital manometer. The manometer was interfaced with a PC so as to automate the acquisition process. The manometer was sampled 500 times through a 16-bit A/D board and averaged to establish the pressure at each location.

A six-component Aerolab sting balance was used for force and moment determination. The accuracy of this balance is estimated at 0.5% of full scale for lift, drag, and pitching moment. Balance resolution is better than 2×10^{-4} of the measured coefficient on all channels. Through repeated data runs, repeatability of the balance for lift, drag, and pitching moment is estimated at $\Delta C_L = 0.0008$, $\Delta C_D = 0.0005$, and $\Delta C_m = 0.0008$. Model pitch and yaw is adjusted using dc motors connected through a potentiometer to a digital read-out display. Model angle of attack can be set to within 0.05 deg. Force balance data as well as tunnel dynamic pressure were acquired using a PC equipped with a 16-bit A/D board.

The data acquisition program used to acquire the balance loads samples each data channel 1000 times and averages it. The code also displays graphically real time lift, drag and pitching moment, such that erroneous data can be quickly recognized.

The force-balance component of the tests comprised pitching the model through a set angle-of-attack range from -2 to 56 deg. Data were recorded at 2-deg intervals. In the vicinity of the maximum lift coefficient, smaller α increments were used where necessary. Pitching moment was taken about 0.25 of the wing's mean aerodynamic chord, effectively the wing's midroot chord. The moment reference length was the mean aerodynamic chord. Delta-wing flows, assuming enforced leading-edge flow separation, are not particularly sensitive to Reynolds number or scale effects, although the location of the secondary separation is Reynolds-number dependent. In an effort to be consistent with other investigations,[19,20] it was decided not to employ any type of forced transition, as enforced transition does not guarantee a flowfield representative of realistic flight Reynolds numbers. Wentz[18] has shown that the vortex breakdown location is indeed insensitive to Reynolds-number effects.

Tare and interference effects were determined using an image system,[21] as this method is relatively simple to implement and yields the total interference and tare effects, and may additionally be used to determine the wind-tunnel flow angularity. The effect of the model support on pitching moment was determined similarly. In this study solid and wake blockage were corrected for using the method of Shindo.[22] Upwash corrections were applied using the method detailed in Pope and Rae.[21]

Due to equipment load limitations, it was necessary to run the flowfield surveys at a freestream velocity of 20 m/s, yielding a Reynolds number of 0.5×10^6 based on the wing's centerline root chord. A seven-hole conical probe was used for the surveys. The probe was moved using a three-component traversing mechanism. The accuracy of this system in positioning is within 0.03 mm. The probe had a diameter of 1.6 mm. Pressures measured by the probe were evaluated using a 32-channel ESP pressure sensor with a measurement range of ±2.5 KPa. Calibration of the ESP was checked by sequentially comparing a reference pressure imposed on each channel against the value measured by a calibrated Air Neotronics micromanometer. Agreement between the micromanometer and the ESP was generally within 1%. Prior to each test the ESP was zeroed to reduce drift. After completing a test, the ESP was again rezeroed to ascertain if the zeroes had drifted significantly. The pressures measured by the ESP were digitized using a 12-bit A/D board. The probe was calibrated using a least-squares calibration routine. The accuracy of the calibration was verified by inclining the probe at various pitch and yaw angles and comparing the predicted and set angles. Consequently, the accuracy of the probe calibration is estimated to be within 0.5 deg at a yaw or pitch angle of 30 deg.

At each survey point in the flowfield, the pressures were sampled 120 times and averaged. After moving to a new point in the flowfield, data measurement was delayed for 3 s to allow the pressures to stabilize. All data were acquired using the AeroView™ data acquisition and analysis code. The surveys were undertaken at $\alpha = 20$ deg, with the probe tracing a rectangular section perpendicular to the wing surface. At each chordwise station a 30×35 grid was used yielding 1050 points in each crossflow plane. The grids extended laterally from 0.2 to 1.2 of the local semispan (see Fig. 1c). For all cases the grids extended vertically to 0.7 of the local semispan. The lower circuit bound of the probe was 3 mm from the wing surface in order to eliminate any possibility of contact caused by flexing of the support members and to reduce interference between the probe and the upper wing surface. The spanwise resolution of the grids was 0.029 and the vertical resolution 0.023 of the local semispan. These values compare favorably to those used in other investigations.[23] All the ϕ variations were surveyed at $x/c_r = 0.3$, 0.5, and 0.7 (0.9, $\phi = 0$ deg) in order to determine the chordwise effects of ϕ on the flowfield.

AeroView was used for processing data from the probe surveys. This included calculation of vorticity and circulation. The code allows the evaluation of circulation using either a surface integral of the vorticity or a line integral of the velocity around a contour enclosing the surface. The total crossflow circulation was evaluated using both these methods for all of the surveyed data, and in no case was the discrepancy greater than 1.5% and was typically <0.2%. This was encouraging as it would be expected that circulation based on vorticity integration may incur a somewhat greater error due to differentiation of the discrete velocity field. The assumption was thus made that the level of uncertainty in the measurement of circulation may be satisfactorily evaluated by determining the uncertainty in the line integral method for determining Γ. Evaluation of various data sets yielded an uncertainty in the measurement of circulation of 0.76%.

Results and Discussion

Forces and Moments

Wentz[18] conducted a comprehensive force-balance investigation of the effects of wing sweep on a range of planar delta wings, with Λ_{pr} ranging from 45 to 85 deg. Wentz's[18] results are often regarded as baseline data and have been used to verify numerous theoretical/computational methodologies. Figure 2 shows comparisons between the present results and those of Wentz[18] for $\Lambda_{\mathrm{pr}} = 70$- and 75-deg delta wings. Theoretical predictions using the method of Polhamus[2] are also included. Agreement between the experimental data sets is seen to be excellent.

The results of wing nonplanarity on lift coefficient are presented in Fig. 3. The effect of anhedral and dihedral is equivalent at low lift coefficients ($\alpha < 10$ deg) showing that the impact of ϕ on the attached flow lift curve slope is weak. Marked lift enhancement effects, both pre- and post-$C_{L\,\max}$, are associated with anhedral (for $\alpha > 10$ deg, with all ϕ variations demonstrating similar performance) when compared to the planar wing. This suggests that the effectiveness of anhedral/deg reduces as anhedral increases, i.e., small ϕ, generate larger lift increases relative to the deflection angle ($\Delta C_L / \Delta \phi$) than large anhedral angles. Increasing the dihedral angle causes ever greater lift loss for a given α compared to the planar wing. Dihedral results in abrupt post-maximum lift behavior, with significant loss of lift compared to the planar wing (see Fig. 3). Anhedral has the opposite effect: post-maximum lift behavior is less abrupt than the planar wing, whereas in addition lift in this region is augmented with significant post-stall lift recovery evident. Wing efficiency may be gauged in terms of $k = \pi \mathrm{AR}(C_D - C_{D\,\min})/C_L^2$, which as already mentioned for this class of wings is given by $k = \pi \mathrm{AR} \tan\alpha / C_L$. Thus for a given combination of AR and α, aerodynamic efficiency can only be improved through an increase in lifting ability. For a constrained span unswept planar wing, k has a theoretical minimum value of 1[8]. For low AR deltas ($\mathrm{AR} = \frac{1}{4}$) and rectangular plates of similar AR, k can be < 1 (Refs. 24 and 25). For nonplanar wings, however, k's value may reduce appreciably below 1[9]. For slender delta wings k typically reduces as α increases due to increased lift from the vortex sheets. Figure 4 clearly shows that anhedral increases efficiency and dihedral decreases efficiency compared to the planar wing, as would be expected considering the disparate lift augmentation of these configurations.

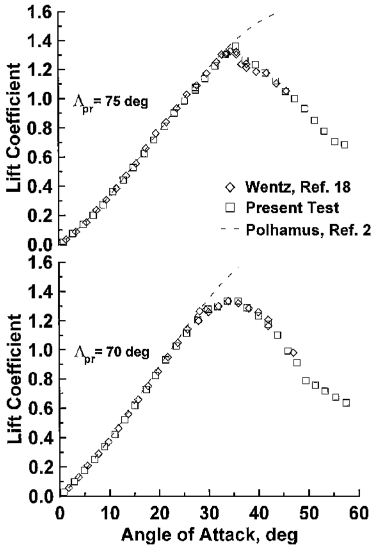

Fig. 2 Comparison of present data with that of Wentz[18] and Polhamus[2] theory.

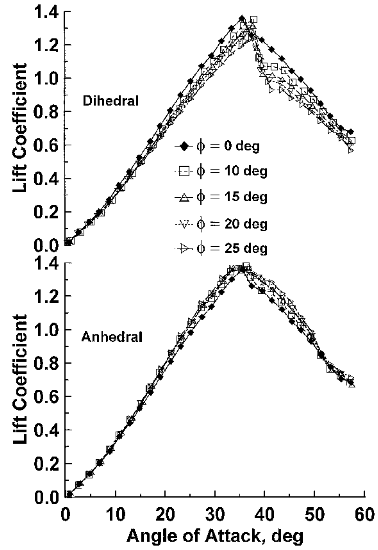

Fig. 3 Effect of ϕ on measured lift coefficient.

Fig. 4 Effect of ϕ on induced efficiency.

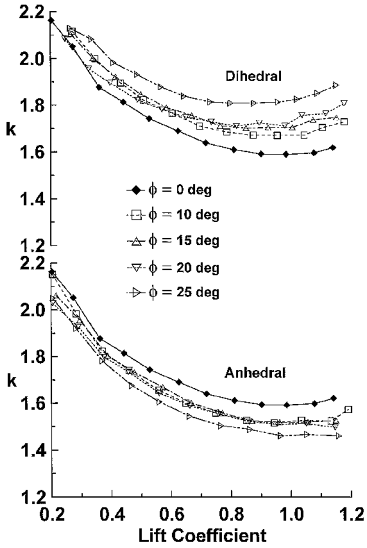

Fig. 5 Effect of ϕ on measured pitching moment coefficient.

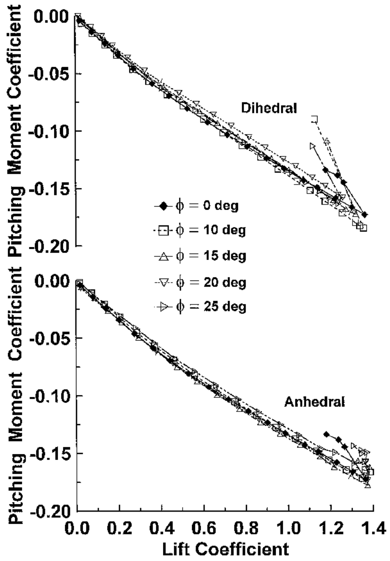

Fig. 6 Effect of ϕ on location of the wing a.c.

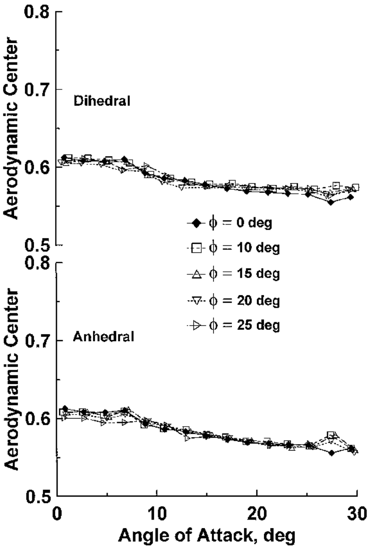

Fig. 7 Effect of ϕ on the spanwise pressure distribution, α = 10 deg.

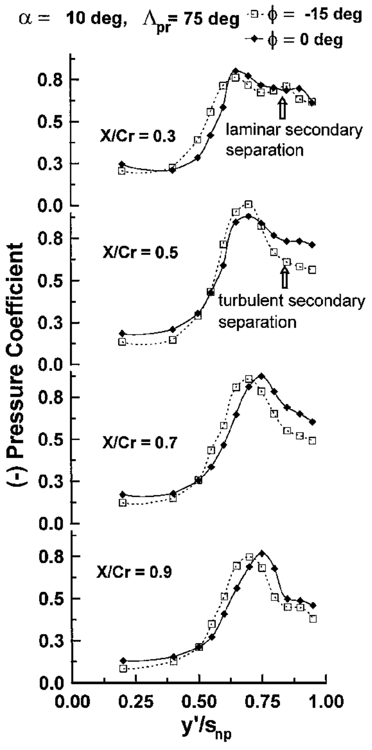

Effects of anhedral and dihedral on the pitching moment coefficient are shown in Fig. 5. The data show that pitch up is coincident with $C_{L\max}$, as is typical for highly swept wings. The effect of anhedral and dihedral on pitching moment is seen to be relatively minimal. This suggests that for this wing geometry modifications to the wing flowfield by either anhedral or dihedral are affected uniformly such that any altered loading follows the load distribution of the projected planar wing.

Figure 6 exhibits the location of the wing's aerodynamic centers (expressed as a fraction of the wing root chord) as a function of α. Thus an aerodynamic center location of 0 corresponds to the wing apex and 1 to the wing trailing edge. Generally, as follows from Fig. 5, the effect of ϕ on the aerodynamic center (a.c.) location is weak. In all instances the aerodynamic center moves forward toward the wing apex with increasing α. This is caused by increasing trailing-edge influence and thus departure from conical flow penetrating further upstream with elevated angle of attack. The trailing-edge effects influence the vortex lift to a greater extent than the potential lift.[26] Consequently, as the vortex lift constitutes an increasingly greater percentage of the total lift as α increases, the a.c. moves forward.

Surface Pressures

The effects of anhedral on surface pressures are summarized in Figs. 7–9, for $\alpha = 10$, 20, and 30 deg, respectively. The pressure data are presented as a function of y'/s_{np}, where s_{np} is the local wing semispan or arc length, i.e., not projected. The most obvious effect of anhedral shown in Fig. 7 is an inboard migration of the vortices relative to the planar wing as evidenced by the suction peak movement. At this α anhedral appears to have a minimal overall effect on the suction peak pressures compared to the planar wing. Transition of the crossflow boundary layer precipitates an outboard movement of the primary vortex suction peak as demonstrated by examination of Fig. 7 (compare the spanwise location of the suction peaks in the top two plots of Fig. 7).[27] Anhedral causes increased loading at $x/c_r = 0.3$ for 15 deg $\leq \alpha \leq$ 25 deg (data for $\alpha = 15$ and 25 deg not shown) compared to the planar wing (see Fig. 8). At this chordwise location $x/c_r = 0.3$, the crossflow upper-surface boundary layer appears to have transitioned for $\phi = -15$ deg but not for $\phi = 0$ deg. The increased loading near the apex may be an artifact of altered vortex structure/properties or trajectory, as the state of the crossflow boundary layer affects the nature of the secondary vortex formation and consequently its effect on the primary vortex. It is unlikely that the increased apex loading is greatly responsible for the majority of the observed lift augmentation with anhedral, as enhanced apex loading would be reflected in the pitching moment data.

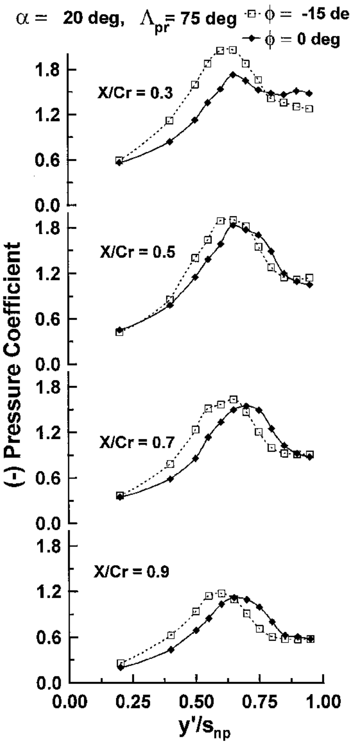

Fig. 8 Effect of ϕ on the spanwise pressure distribution, α = 20 deg.

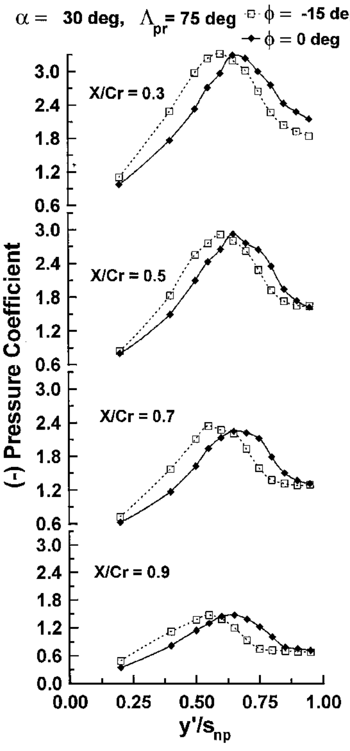

Fig. 9 Effect of ϕ on the spanwise pressure distribution, α = 30 deg.

Raising α to 30 deg (Fig. 9) shows an apparent reduction in relative loading toward the wing apex ($x/c_r = 0.3$) compared to that seen at lower α. For this case both the secondary separation from the planar and nonplanar wing are turbulent, suggesting that the increase in peak loading toward the wing apex noted at lower α (Fig. 8) may be an artifact of the state of the boundary layer. Transition typically causes an increase in the loading associated with the primary vortex (due to an altered vortex trajectory resulting in closer surface proximity) caused by a weaker secondary vortex. Figure 9 shows that the increased lift associated with anhedral in this application is as a result of increased loading inboard relative to the planar wing, and not through any obvious increase in peak loading. For the cases presented the nonplanar wing effectively shifts the vortices further inboard than the planar wing. As a consequence, anhedral has the effect of increasing loading inboard and reducing it outboard, a flow modification favorable for wing root bending moment considerations. In all of the presented cases, apart from $x/c_r = 0.3$ (15 deg $\leq \alpha \leq$ 25 deg), anhedral appears to have a marginal effect on the magnitude of the minimum pressure coefficient relative to the planar wing. Figures 7–9 clearly show the progressive impact of the trailing-edge Kutta condition. With increasing α trailing-edge effects become more marked, with a significant reduction in loading toward the wings' trailing-edge, (see Figs. 8 and 9) evident. The preceding discussion assumes that the wings' lower surface pressures, which were not measured, are relatively independent of ϕ.

Flowfield Properties

Effects of anhedral and dihedral on flowfield properties are displayed in Figs. 10–19. It was necessary to determine if the presence of the seven-hole probe over the upper wing surface may have, in certain cases, precipitated the onset of BD. Payne[28] has shown that the presence of a probe can affect the location of vortex burst, particularly when the burst is near the wing's trailing edge. However, when the probe is not in close proximity to the burst location, its influence is minimal.[28] For the data presented it is unlikely that BD was present over any of the configurations as will be shown in the subsequent discussion and BD trajectories. Figure 10 presents the effect of ϕ on the lateral (y'/s_{np}) and vertical (z'/s_{np}) location of the vortex core with z' orientated perpendicular to the wing chord plane. The vortex core was identified as the region of maximum stagnation pressure loss and highest axial velocity. Upstream of BD these regions are coincident,[29] as was also observed in the present study. This is not, however, the case downstream of burst.[29] In all of the present tests, the maxima of axial velocity and the maximum

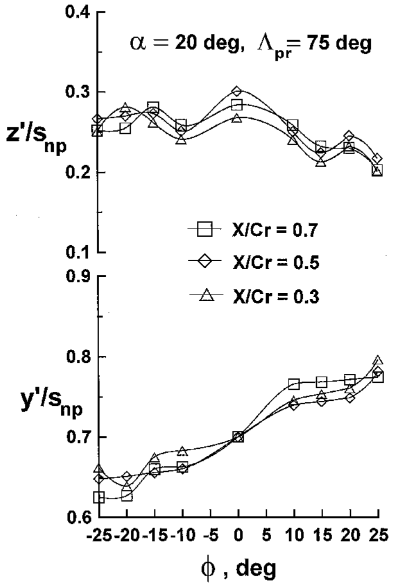

Fig. 10 Effect of ϕ and x/c_r on the vertical and lateral vortex location.

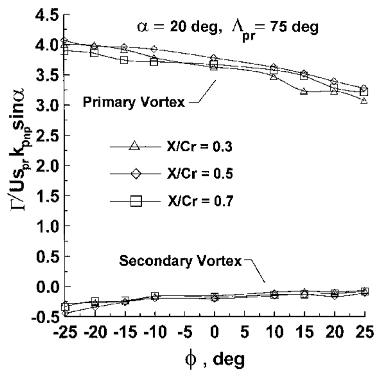

Fig. 11 Effect of ϕ and x/c_r on the maximum vortex circulation.

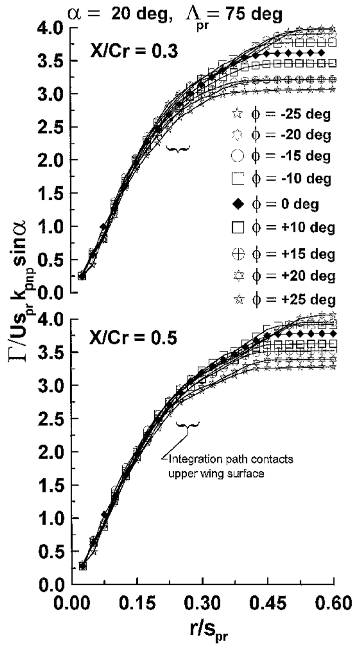

Fig. 12 Effect of ϕ and x/c_r on the radial distribution of vortex circulation.

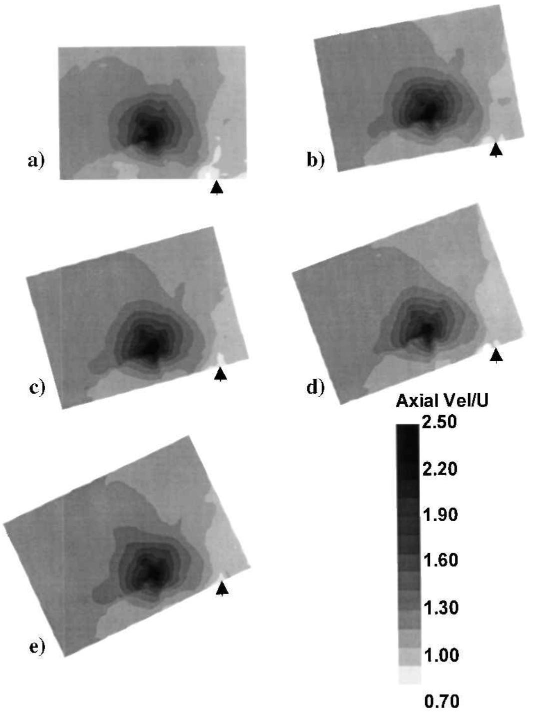

Fig. 14 Effect of dihedral on the vortex axial velocity, x/c_r = 0.5, α = 20 deg. Arrow indicates wing leading edge. ϕ = a) 0, b) 10, c) 15, d) 20, and e) 25 deg.

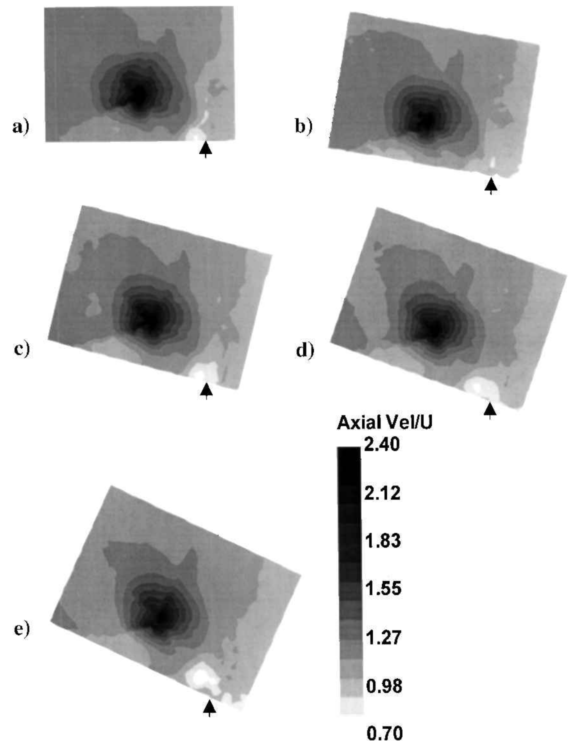

Fig. 13 Effect of anhedral on the vortex axial velocity, x/c_r = 0.5, α = 20 deg. Arrow indicates wing leading edge. ϕ = a) 0, b) − 10, c) − 15, d) − 20, and e) − 25 deg.

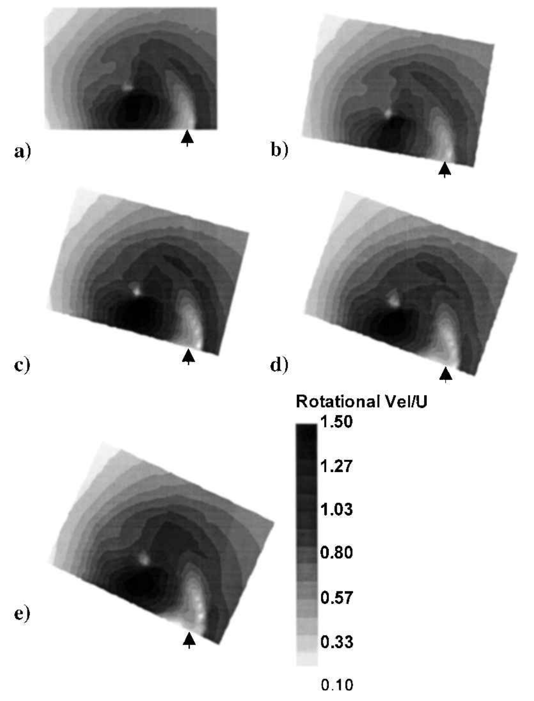

Fig. 15 Effect of anhedral on the vortex rotational velocity, x/c_r = 0.5, α = 20 deg. Arrow indicates wing leading edge. ϕ = a) 0, b) − 10, c) − 15, d) − 20, and e) − 25 deg.

stagnation pressure loss showed coincidence. This concurrence reinforces the presumption that the probe did not initiate premature BD. Data are presented for three chordwise locations to highlight any axial trajectory variations. As shown in Fig. 10, anhedral and dihedral draw the vortex closer to the wing surface. The effect is somewhat discontinuous, with two sequential displacement minima for both + and $-\phi$. The data show that for this wing configuration dihedral draws the vortex comparatively closer to the wing surface than anhedral. Trends regarding chordwise trajectory variations are not clearly apparent, although the most forward survey station ($x/c_r = 0.3$) shows the closest wing-vortex proximity. The lateral vortex location appears sensitive for $\phi \neq 0$ deg, whereas for $\phi = 0$ deg the vortex core trajectory follows a spanwise ray lying along 70% of the local semispan for the flow planes surveyed. As discussed prior and shown in Fig. 10, anhedral pulls the vortex inboard, and dihedral moves the vortex towards the leading edge compared to $\phi = 0$ deg. This effect is most pronounced for initial ϕ, e.g., ±10 deg (similar to the trends seen for the lift dependence on ϕ), with further increases in anhedral/dihedral affecting the vortex trajectory to a lesser degree.

As already mentioned, circulation was calculated using both the spatially integrated vorticity field and the crossflow velocity

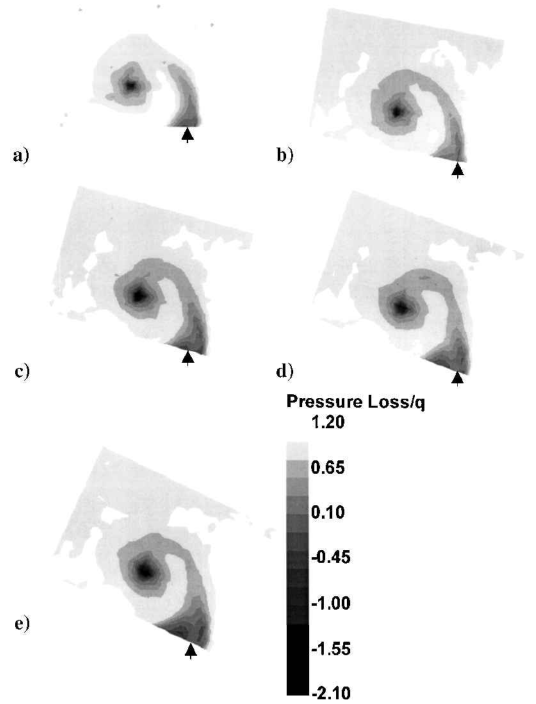

Fig. 16 Effect of anhedral on the vortex pressure loss, x/c_r = 0.5, α = 20 deg. Arrow indicates wing leading edge. ϕ = a) 0, b) − 10, c) − 15, d) − 20, and e) − 25 deg.

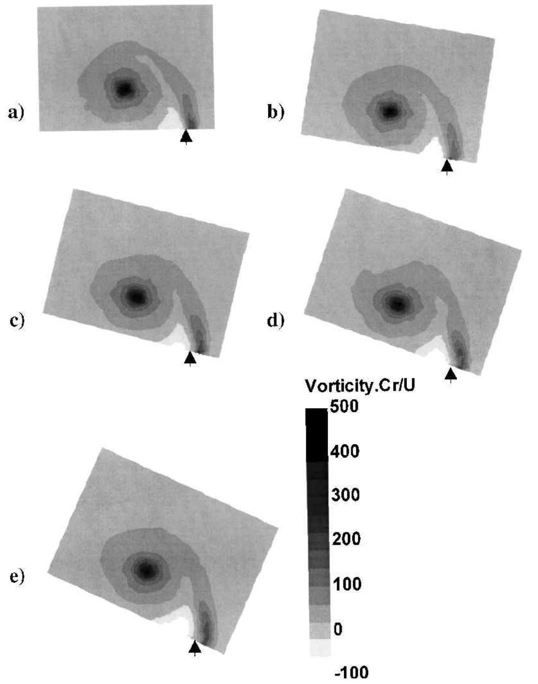

Fig. 18 Effect of anhedral on the vortex axial vorticity, x/c_r = 0.5, α = 20 deg. Arrow indicates wing leading edge. ϕ = a) 0, b) − 10, c) − 15, d) − 20, and e) − 25 deg.

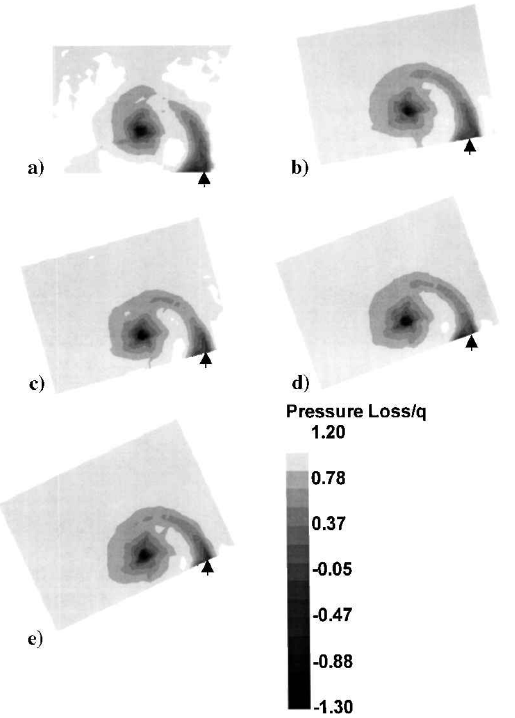

Fig. 17 Effect of dihedral on the vortex pressure loss, x/c_r = 0.5, α = 20 deg. Arrow indicates wing leading edge. ϕ = a) 0, b) 10, c) 15, d) 20, and e) 25 deg.

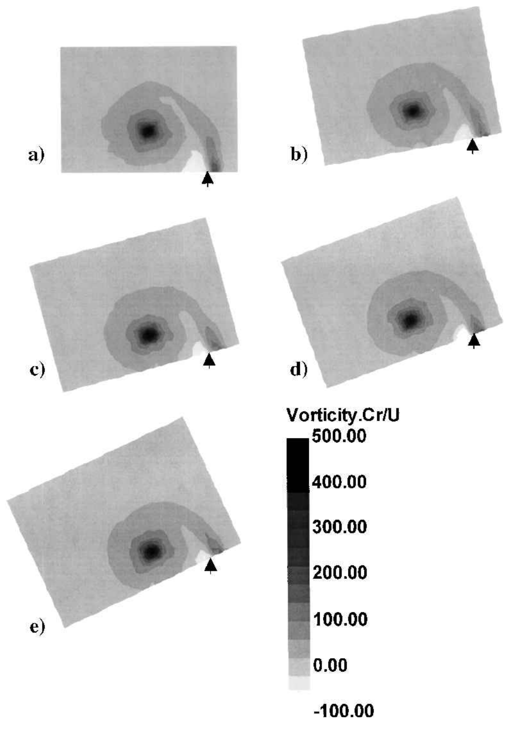

Fig. 19 Effect of dihedral on the vortex axial vorticity, x/c_r = 0.5, α = 20 deg. Arrow indicates wing leading edge. ϕ = a) 0, b) 10, c) 15, d) 20, and e) 25 deg.

components. The two methods showed excellent agreement indicating minimal error in differentiating the velocity field. Consequently, all radial circulation distributions were calculated through vorticity integration. Vorticity integration to compute Γ was also chosen to limit possible errors that probe proximity to the wing surface may have had on the crossflow velocity components when the integration bound encompassed the upper wing surface. Vorticity integration also allows straightforward determination of regions of positive and negative circulation. The integrations proceeded from the vortex core center, i.e., $r = 0$, to $r/s_{\mathrm{pr}} = 0.6$ in $[\Delta(r/s_{\mathrm{pr}}) =]$ 0.025 intervals. The integration path for each r/s_{pr} value was circular. When the integration path impinged on the upper wing surface, the wing was taken as the lower integration path, similarly for the edges of the survey grid. In Ref. 30 it is shown that vortex strength is proportional to k_p and $\sin\alpha$, whereas its chordwise growth is very nearly conical, i.e., proportional to the local semispan. Consequently, to aid in interpretation and characterization, plots depicting circulation have been nondimensionalized by $s_{\mathrm{pr}} U k_{P_{\mathrm{np}}} \sin\alpha$, where $k_{P_{\mathrm{np}}}$ is the lift curve slope of the nonplanar wing. The circulation of the primary vortex was assumed to contain only positive vorticity (the right-hand-side wing panel was surveyed), whereas the secondary vortex was assumed to contain all of the negative vorticity. The effect of ϕ and x/c_r on the total measured strength of the primary and secondary vortices is summarized in Fig. 11. The data were acquired at $\alpha = 20$ deg. To ascertain any chordwise variation in circulation, data are presented for survey planes located at $x/c_r = 0.3$, 0.5, and 0.7. The figure shows that the circulation is relatively conical (i.e., $\propto s$) as it falls into a thin band for the three chordwise survey locations for a given ϕ. The secondary vortex also shows conical flow development, with similar levels of circulation developed for each ϕ value at the three survey stations (remember that the circulation is scaled by the local semispan). The strength of the primary vortex decreases continuously as ϕ is varied from -25 to $+25$ deg. Thus anhedral increases the total vortex strength relative to the planar wing, whereas dihedral reduces it. The variation of the circulation with ϕ for this wing geometry appears relatively linear. The secondary vortex is seen to constitute approximately 7% of the strength of the primary vortex.

The impact of ϕ on vortex radial development is summarized in Fig. 12 for $\alpha = 20$ deg. The radial distribution shows that dihedral has a greater effect on vortex strength than anhedral. Generally, for the data range tested increasing anhedral increases total vortex circulation compared to $\phi = 0$ deg, whereas the opposite is true for dihedral due in part to an increase and decrease in length of the shear layer, respectively. It is evident that the magnitude of the effect of ϕ is asymmetric with respect to anhedral or dihedral. Dihedral affects vortex strength markedly for $r/s_{\mathrm{pr}} > 0.22$, i.e., for regions where $r/s_{\mathrm{pr}} >$ than the location where the integration path contacts the wing. Until the path contacts the surface the vortex circulation increases radially through the addition of relatively axisymmetric vorticity centered around the core. However, beyond the contact point, additional circulation is added only through vorticity contained in the leading-edge shear layer. Consequently, the rate of increase of radial circulation diminishes markedly. The effects of anhedral are mainly confined to the leading-edge shear layer (compared to the planar wing). Increasing anhedral results in the maximum circulation being reached at progressively higher r/s_{pr} values, implying a larger vortex and/or longer shear layer, which is consistent with the observed inboard vortex movement with anhedral. Comparison of the data for $x/c_r = 0.3$ and 0.5 does suggest a moderate axial location influence. Dispersion amongs the curves is seen to reduce with increasing distance from the wing apex. Notice that Γ increases relatively linearly for $r/s_{\mathrm{pr}} < 0.2$ such that the integrated vorticity comprises the rotational region surrounding the vortex core and does not include the leading-edge shear layer. This would imply a radial distribution of vorticity $\propto 1/r$, with viscous effects keeping the vorticity finite for $r = 0$. A linear variation of radial circulation is not without precedent: Lowson[31] found in a low-speed wind-tunnel study of the flow over a 75-deg delta that the transverse velocity in the core was uniform so by corroborating the theoretical predictions of Mangler and Smith.[32] Thus, in this case, the vortex strength is simply a linear function of the core dimensions.

Vortex axial velocity profiles are shown in Figs. 13 and 14. The data are nondimensionalized by the freestream velocity. High axial velocities, showing the jetting nature of the vortex core, are visible in Figs. 13 and 14. The secondary vortex is discernible as a white region adjacent to the wing leading edge and is characterized by velocities below the freestream—a wake-type vortex. The flow region encompassing the secondary vortex recorded the lowest axial velocities in the measurement plane for all tests. Notice that the core axial velocity profiles show reasonable axisymmetry for anhedral, but the velocity profile becomes laterally elongated with dihedral. This may, in part, be caused by the outboard migration of the leading-edge vortices associated with dihedral (see Fig. 10). As the survey plane was perpendicular to the wing centerline, an outboard movement of the vortex would result in an increased misalignment between the measurement plane and the vortex. The spatial extent of the secondary vortex wake-type flow increases with anhedral (Fig. 13): this characteristic is not evident for dihedral (Fig. 14). Figures 13 and 14 also show that the leading-edge shear layer initially convects axially at or just above the freestream velocity. View Figs. 18 and 19 for location of the shear layer. Visser and Nelson[33] measured the flowfield over a planar 75-deg delta wing at $\alpha = 20$ deg. Their data, for similar conditions to those presented, indicate a peak axial velocity of 2.33 compared to 2.39 from the present study, a difference of 2.5%. Table 1 comprises a summary of the effect of ϕ on vortex properties. The data show the chordwise variation of the measured maximum axial velocity to be relatively small, demonstrating the conical nature of the flow. A similar trend is also present for the secondary vortex, corresponding to the minimum measured axial velocity.

Table 1 Chordwise effects of wing nonplanarity on vortex aerodynamic parameters, $\Lambda_{\mathrm{pr}} = 75$ deg, $\alpha = 20$ deg

x/c_r	ϕ, deg	$\omega_{\max} c_r/U$	C_{pt}	$V_{A\,\min}/U$	$V_{A\,\max}/U$
0.3	0	678.7	−1.29	0.78	2.17
0.5	0	485.1	−1.30	0.79	2.39
0.7	0	388.3	−1.69	0.85	2.44
0.9	0	303.8	−1.20	0.66	2.38
0.3	−15	682.2	−1.94	0.78	2.16
0.5	−15	435.7	−1.88	0.78	2.24
0.7	−15	363.6	−1.96	0.76	2.34
0.3	15	706.0	−1.25	0.94	2.25
0.5	15	500.8	−1.27	0.79	2.46
0.7	15	397.9	−1.41	0.84	2.48

Crossflow rotational velocities are presented in Fig. 15 for $\phi \leq 0$ deg. The rotational velocity is defined as $(v^2 + w^2)^{0.5}$. If the vortex was axisymmetric and contained no radial velocity components, the figures should contain concentric circles for isorotational velocity contours. However, this is clearly not the case and is indicative of radial inflow velocities as a result of the low pressures experienced along the vortex core.[34] The center of the vortex is clearly visible as a white mark, indicating zero rotational velocity. The data do not show any marked effect of nonplanarity on the rotational velocity distribution. Similar data for $\phi > 0$ deg are not presented as the observed effect of ϕ on the data was small. The highest rotational velocities are located between the vortex core and the upper wing surface due to the flow being rotationally asymmetric. This is shown computationally[35] by Longo. Such a feature also indicates that the spanwise velocity component is considerably greater than the vertical velocity component because of the channel formed between the vortex core and the wing surface.[35] This channel causes an acceleration of the vortical flow in the spanwise direction that causes radial forces. As a result, the vortex core deforms due to the differential centrifugal forces acting on the top and bottom of the vortex.[35] Comparison of Figs. 15 and 18 shows that the region of low rotational velocity, indicated by the white streak adjacent to the wing leading edge, is located at the approximate center of the shear layer. This indicates a substantial velocity gradient across the shear layer, which is a manifestation of the large shear layer vorticity. The origin of these velocity gradients are the disparate spanwise outflow velocities of the upper and lower surface boundary layers. Figure 15 also suggests that the rotational velocities of the secondary vortices are generally low.

The region of highest rotational velocity is also seen to be somewhat below and to the right of the vortex core for all cases. It is probable that the highest rotational velocities are situated somewhat outboard of the primary vortex due to the combined induced velocities of both the primary and secondary vortices causing the rotational velocity maxima. Longo's[35] results for rotational velocity isosurfaces do not show this spanwise displacement of the velocity maxima relative to the vortex core. Longo's results are, however, inviscid, thus the secondary vortex was not present in the computations.

Anhedral/dihedral effects on the total pressure loss are displayed in Figs. 16 and 17. The pressure loss is defined as the difference between the local stagnation pressure and the freestream static pressure. Figure 16 and Table 1 clearly show that anhedral increases the core stagnation pressure loss compared to the planar wing. Anhedral is seen to increase the spatial extent of pressure loss adjacent to the wing leading edge comprising the leading-edge shear layer and secondary vortex, whereas the opposite effect is seen for dihedral (Fig. 17). The regions showing the greatest pressure losses are near the wing leading-edge and the core. The pressure losses at the vortex core are largest due to accumulated viscous losses.[34] The large radial gradients evident in the pressure loss contours are a manifestation of misalignment between the vorticity and velocity vectors. This follows from Crocco's theorem assuming steady inviscid adiabatic flow. Misalignment is indicated by large core rotational velocities combined with a vorticity vector, which is essentially axial.

Vector misalignment as the main cause of pressure loss is also suggested by the results of Ref. 36, where the flow over a delta wing was forced to sustain zero pressure loss, which resulted in alignment of the vorticity and velocity vectors. The data in Table 1 show that the axial variation of the maximum pressure loss is approximately constant for a given wing within the experimental accuracy. This result was also reported by Kegelman and Roos.[29]

Measurements of the effect of anhedral/dihedral on axial vorticity are presented in Figs. 18 and 19. The axial vorticity was determined from the crossflow velocity components perpendicular to the wing surface. To enhance the contrast in the figures, the negative vorticity scale was fixed at -100. Thus, the white regions adjacent to the wing leading edge indicate the size and location of the secondary vortex, but not its relative magnitude. Both Figs. 18 and 19 indicate that nonplanarity has a moderate effect on the core axial vorticity, where the majority of the axial vorticity is concentrated. As cited previously, Visser and Nelson's[33] results for a planar $\Lambda_{\mathrm{pr}} = 75$-deg wing at $\alpha = 20$ deg yielded a peak core axial vorticity of 517, which compares favorably with that determined in the present study, i.e., 485. Figure 18 shows that increasing anhedral also increases the spatial extent of strengthened vorticity along the leading-edge shear layer compared to the planar wing. This may be caused by anhedral effectively rotating the wing leading edge down (considering a side projection), thus increasing the duration that the leading-edge vorticity vector is approximately aligned perpendicular to the measurement plane,[37] as the vorticity vector that leaves the wing leading edge is initially parallel to that edge. Figure 18 shows that increasing anhedral significantly increases the spatial extent of negative vorticity, i.e., the secondary separation vortex, probably caused by the inboard movement of the primary vortex with anhedral. The feeding sheet for the anhedral configurations is increased in length due to inboard movement of the vortex with anhedral. Dihedral (see Fig. 19), results in less lateral deformation of the vortex than anhedral. The leading-edge shear layer also appears to have its strength attenuated compared to the planar wing. The core of the vortex is situated closer to the wing surface than for $\phi = 0$ deg. In contrast with anhedral, dihedral reduces the spatial extent of the secondary vortex because of the closer vortex–shear-layer proximity, but not necessarily its peak vorticity (data omitted for brevity). Although the probe surveys were undertaken at a single fixed α ($= 20$ deg), the nature of the flow development on a delta wing suggests that the features described should be applicable at higher incidence in prevortex BD flow. The effects of higher incidence would be to strengthen the vortices, increase their size, and usually to displace the cores' trajectories inboard (see Figs. 7–9).

Vortex-Burst Trajectories

The effects of anhedral/dihedral on vortex burst trajectories are summarized in Fig. 20. The data were acquired at $Re = 0.15 \times 10^6$ based on c_r. The wings were carefully aligned to minimize burst asymmetry of the left- and right-hand-side vortices. However, as asymmetry is extremely sensitive to yaw and roll, slight model imperfections are capable of instigating asymmetry. Consequently, all of the presented data represent an average of the left- and right-hand-side vortex-burst locations. Highly swept delta wings are also prone to a chordwise oscillation of the burst location. To moderate the impact of the oscillations on the results, the burst trajectories were recorded on video. The burst location was then subsequently averaged for each α. Nonetheless, the asymmetry and chordwise oscillations do introduce an uncertainty into the results. Thus the plots have a conservative or worst-case uncertainty bound included; it is expected that the uncertainty is somewhat less than that indicated. The burst trajectories were not corrected for wall effects as at present an accepted method to correct the trajectories for the tested wing configurations is not available. The effect of the tunnel walls would be to decrease the α at which breakdown occurs at a specific chordwise location[38] due to the upwash from the image leading-edge vortices that simulate the tunnel side walls. Thus a correction to account for the tunnel side walls would comprise an increment to the wing's geometric α. It would be expected that the upwash corrections for all of the wings investigated would be of similar magnitude as the effect of anhedral and dihedral on the vortex strength was moderate.

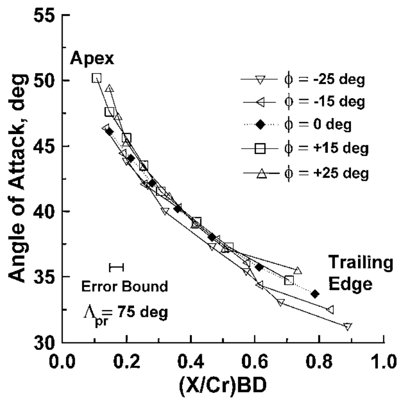

Fig. 20 Effect of ϕ on vortex-burst trajectory.

The data in Fig. 20 clearly indicate that within the experimental accuracy the effects of anhedral and dihedral on vortex burst are marginal. A similar result was found by Washburn and Gloss[15] for the vortices over a circular arc spanwise cambered 76-deg leading-edge sweep delta wing compared to an equal projected span planar wing. This result may be anticipated for the current models since there is a weak dependency of $C_{P\,\mathrm{min}}$ and vortex core properties on ϕ. Core properties have been used successfully in the Rossby number criterion (the ratio of peak core axial velocity to the rotational velocity at the edge of the viscous core) to predict vortex breakdown in numerical codes.

Conclusions

An experimental investigation into the effects of anhedral and dihedral on a 75-deg sweep delta wing was undertaken. Testing encompassed force balance, surface-pressure measurement, seven-hole probe surveys, and the determination of vortex-burst trajectories. From the experimental data the following conclusions are drawn:

The net effect of nonplanarity is an increase in lift for anhedral and a decrease in lift for dihedral compared to the planar wing. Consequently, anhedral shows the greatest benefit for most applications. Small anhedral angles are most effective in augmenting lift. Anhedral increases wing efficiency over a comparative planar wing. Anhedral does not appear to greatly augment the strength of the leading-edge vortex. The major benefit from anhedral would appear to be caused by its displacing effect on the vortex trajectory, both drawing it closer to the wing surface and inboard. As the vortex is drawn inboard, its induced surface loading acts on a greater area of the wing. Dihedral also draws the vortex closer to the wing surface (to a greater extent then anhedral) with a concomitant displacement of the vortex towards the wing leading edge. Anhedral does not appear to introduce any detrimental effects on longitudinal stability and does not incur any penalties in terms of vortex-burst characteristics.

References

[1] Winter, H., "Stromungsvorgangean Platten und Profilierten Korpern beil Kleinen Spannweiten," *Forschung auf dem Gebiete des Ingenieur-Wesens*, Vol. 6, No. 2, 1935, pp. 67–71.

[2] Polhamus, E. C., "A Concept of the Vortex Lift of Sharp-Edge Delta Wings Based on a Leading-Edge Suction Analogy," NASA TN D-3767, Oct. 1966.

[3] Lamar, J. E., "Subsonic Vortex-Flow Design Study for Slender Wings," *Journal of Aircraft*, Vol. 15, No. 9, 1978, pp. 611–617.

[4] Lee, G. H., "Reduction of Lift-Dependent Drag with Separated Flow," A.R.C., CP 593, 1962.

[5] Traub, L. W., "Effects of Spanwise Blowing on a Delta Wing with Vortex Flaps," *Journal of Aircraft*, Vol. 32, No. 4, 1995, pp. 884–887.

[6] Rinoie, K., and Stollery, J. L., "Experimental Studies of Vortex Flaps and Vortex Plates; Part 2. 1.15m Span 60° Delta Wing," National Aerospace Lab., TR-1180T, Tokyo, Japan, Oct. 1992.

[7] Lamar, J. E., and Campbell, J. F., "Vortex Flaps—Advanced Control Devices for Supercruise Fighters," *Aerospace America*, Jan. 1984, pp. 95–99.

[8] Munk, M. M., "The Minimum Induced Drag of Aerofoils," NACA Rept. 121, 1921.

[9] Cone, C. D., "The Theory of Induced Lift and Minimum Induced Drag of Nonplanar Lifting Systems," NASA TR R-139, Feb. 1962.

[10] Lowson, M. V., "Minimum Induced Drag for Wings with Spanwise Camber," *Journal of Aircraft*, Vol. 27, No. 7, 1990, pp. 627–631.

[11] Squire, L. C., "Camber Effects on the Non-Linear Lift of Slender Wings with Sharp Leading-Edges," A.R.C., C.P. 924, 1966.

[12] Brown, C. E., and Michael, W. H., "On Slender Delta Wings with Leading-Edge Separation," NACA TN 3135, 1955.

[13] Queijo, M. J., and Jaquet, B. M., "Investigation of Effects of Geometric Dihedral on Low-Speed Static Stability and Yawing Characteristics of an Untapered 45 Degree Sweptback-Wing Model of an Aspect Ratio 2.61," NACA TN 1668, Sept. 1948.

[14] Maggin, B., and Shanks, R. E., "The Effect of Geometric Dihedral on the Aerodynamic Characteristics of a 40 Degree Swept-Back Wing of Aspect Ratio 3," NACA TN 1169, Dec. 1946.

[15] Washburn, K. E., and Gloss, B. B., "The Effects of Wing Dihedral and Section Suction Distribution on Vortex Bursting," NASA TM X-72745, July, 1975.

[16] Washburn, K. E., and Gloss, B. B., "Effect of Wing-Tip Dihedral on the Longitudinal and Lateral Aerodynamic Characteristics of a Supersonic Cruise Configuration at Subsonic Speeds," NASA TM X-72693, Aug. 1976.

[17] Kegelman, J. T., and Roos, F. W., "Effects of Leading-Edge Shape and Vortex Bursts on the Flowfield on a 70-Deg-Sweep Delta Wings," AIAA Paper 89-0086, Jan. 1989.

[18] Wentz, W. H., Jr., and Kohlman, D. L., "Wind Tunnel Investigation of Vortex Breakdown on Slender Sharp-Edged Wings," NASA CR 98737, Nov. 1968.

[19] Kirby, D. A., "An Experimental Investigation of the Effect of Planform Shape on the Subsonic Longitudinal Stability Characteristics of Slender Wings," A.R.C., R&M 3568, 1969.

[20] Peckham, D. H., "Low Speed Wind Tunnel Tests on a Series of Uncambered Slender Pointed Wings with Sharp Edges," A.R.C., R&M 3186, 1961.

[21] Pope, A., and Rae, W. H., *Low-Speed Wind Tunnel Testing*, Wiley, New York, 1984, pp. 199–208, 362–424.

[22] Shindo, S., "Simplified Tunnel Correction Method," *Journal of Aircraft*, Vol. 32, No. 4, 1995, pp. 210–213.

[23] Nelson, R. C., and Visser, K. D., "Breaking Down the Delta Wing Vortex—The Role of Vorticity in the Breakdown Process," AGARD Symposium on Vortex Flow Aerodynamics, Paper 21, CP-494, Oct. 1990.

[24] Fox, C. H., and Lamar, J. E., "Theoretical and Experimental Longitudinal Aerodynamic Characteristics of an Aspect Ratio 0.25 Sharp-Edge Delta Wing at Subsonic, Supersonic and Hypersonic Speeds," NASA TN D-7651, 1974.

[25] Lamar, J. E., "Extension of the Leading-Edge Suction Analogy to Wings with Separated Flow Around the Side Edges at Subsonic Speeds," NASA TR R-428, 1974.

[26] Kirpatrick, D. L. I., "Analysis of the Static Pressure Distribution on a Delta Wing in Subsonic Flow," ARC, R&M 3619, London, 1970.

[27] Kuchemann, D., *The Aerodynamic Design of Aircraft*, Pergamon, London, 1978, p. 391.

[28] Payne, F. M., "The Structure of Leading-Edge Vortex Flows Including Breakdown," Ph.D. Dissertation, Dept. of Aerospace and Mechanical Engineering, Univ. of Notre Dame, Notre Dame, IN, May 1987.

[29] Kegelman, J. T., and Roos, F. W., "The Flowfields of Bursting Vortices over Moderately Swept Delta Wings," AIAA Paper 90-0599, Jan. 1990.

[30] Traub, L. W., "Prediction of Delta Wing Leading-Edge Vortex Circulation and Lift-Curve Slope," *Journal of Aircraft*, Vol. 34, No. 3, 1997, pp. 450–452.

[31] Lowson, M. V., "Visualization Measurements of Vortex Flows," *Journal of Aircraft*, Vol. 28, No. 5, 1991, pp. 320–327.

[32] Mangler, K. W., and Smith, J. H. B., "A Theory For the Flow Past a Slender Delta Wing with Leading-Edge Separation," *Proceedings of the Royal Society A*, Vol. 251, 1959, pp. 200–217.

[33] Visser, K. D., and Nelson, R. C., "Measurements of Circulation and Vorticity in the Leading-Edge Vortex of a Delta Wing," *AIAA Journal*, Vol. 31, No. 1, 1993, pp. 104–111.

[34] Verhaagen, N. G., and Kruisbrink, A. C. H., "Entrainment Effect of a Leading-Edge Vortex," *AIAA Journal*, Vol. 25, No. 8, 1987, pp. 1025–1032.

[35] Longo, J. M. A., "Compressible Invisicid Vortex Flow of a Sharp Edge Delta Wing," *AIAA Journal*, Vol. 33 No. 4, 1995, pp. 680–687.

[36] Newsome, R. W., and Kandil, O. A., "Vortical Flow Aerodynamics—Physical Aspects and Numerical Simulation," AIAA Paper 87-0205, Jan. 1987.

[37] Traub, L. W., "Effects of Spanwise Camber on Delta Wing Aerodynamics: An Experimental and Theoretical Investigation," Ph.D. Dissertation, Aerospace Engineering Dept., Texas A&M Univ., College Station, TX, May 1999.

[38] Traub, L. W., "Prediction of Tunnel Wall Upwash for Delta Wings Including Vortex Breakdown Effects," *Aeronautical Journal*, Vol. 103, No. 1021, 1999, pp. 139–142.